



Gernon, T., Hincks, T. K., Tyrrell, T., Rholing, E., & Palmer, M. (2016). Snowball Earth ocean chemistry driven by extensive ridge volcanism during Rodinia breakup. *Nature Geoscience*, 9(3), 242-248. DOI: 10.1038/ngeo2632

Peer reviewed version

Link to published version (if available):  
[10.1038/ngeo2632](https://doi.org/10.1038/ngeo2632)

[Link to publication record in Explore Bristol Research](#)  
PDF-document

This is the author accepted manuscript (AAM). The final published version (version of record) is available online via Nature at <http://www.nature.com/ngeo/journal/v9/n3/full/ngeo2632.html>. Please refer to any applicable terms of use of the publisher.

## **University of Bristol - Explore Bristol Research**

### **General rights**

This document is made available in accordance with publisher policies. Please cite only the published version using the reference above. Full terms of use are available:  
<http://www.bristol.ac.uk/pure/about/ebr-terms.html>

1           **Snowball Earth ocean chemistry driven by extensive ridge**  
2                           **volcanism during Rodinia breakup**

3    T. M. Gernon <sup>a,\*</sup>, T. K. Hincks <sup>b</sup>, T. Tyrrell <sup>a</sup>, E. J. Rohling <sup>a,c</sup>, M. R. Palmer <sup>a</sup>

4    <sup>a</sup>*Ocean and Earth Science, University of Southampton, European Way, Southampton SO14 3ZH, U.K.*

5                   <sup>b</sup>*School of Earth Sciences, University of Bristol, Bristol, BS8 1RJ, U.K.*

6    <sup>c</sup>*Research School of Earth Sciences, The Australian National University, Canberra, ACT. 2601, Australia*

---

7    **Abstract**

8    **During Neoproterozoic Snowball Earth glaciations, the oceans gained**  
9    **massive amounts of alkalinity, culminating in the deposition of massive**  
10   **cap carbonates upon deglaciation. Changes in terrestrial runoff associ-**  
11   **ated with both breakup of the Rodinia supercontinent and deglaciation**  
12   **can explain some, but not all of the requisite changes in ocean chem-**  
13   **istry. Submarine volcanism along shallow ridges formed during super-**  
14   **continent breakup results in the formation of large volumes of glassy**  
15   **hyaloclastite, which readily alters to palagonite. Here we estimate fluxes**  
16   **of calcium, magnesium, phosphorus, silica and bicarbonate associated**  
17   **with these shallow ridge processes, and argue that extensive submarine**  
18   **volcanism during the breakup of Rodinia made an important contribu-**  
19   **tion to changes in ocean chemistry during Snowball Earth glaciations. We**  
20   **use Monte Carlo simulations to show widespread hyaloclastite alteration**  
21   **under near-global sea ice cover could lead to Ca<sup>2+</sup> and Mg<sup>2+</sup> supersat-**  
22   **uration over the course of the glaciation that is sufficient to explain the**  
23   **volume of cap carbonates deposited. Furthermore, our conservative esti-**  
24   **mates of phosphorus release are sufficient to explain the observed P:Fe**  
25   **ratios in sedimentary iron formations from this time. This large phospho-**  
26   **rus release may have fuelled primary productivity, which in turn would**  
27   **have contributed to atmospheric O<sub>2</sub> rises that followed Snowball Earth**  
28   **episodes.**

---

\* Corresponding author.

*Email address:* Thomas.Gernon@noc.soton.ac.uk (T. M. Gernon).

29 Breakup of the Rodinia supercontinent contributed to profound environmen-  
30 tal change during the Neoproterozoic ( $\sim 1000$ – $540$  Ma). It is thought that  
31 ice-sheets reached the equator<sup>1,2</sup> and global temperatures dropped to  $-50^\circ\text{C}$   
32 during two long-lived ‘snowball’ events: the Sturtian (Cryogenian) glaciation  
33 at *c.* 720–660 Ma and the Marinoan (Varanger) glaciation at *c.* 650–630 Ma.  
34 These globally distributed glaciations have been attributed to major conti-  
35 nental reconfiguration episodes<sup>3,4</sup>. Protracted rifting around *c.* 750<sup>3</sup>–725 Ma<sup>5</sup>  
36 (lasting 100–120 Myr) formed the Proto-Pacific Ocean (Fig. 1a). The Sturtian  
37 glaciation coincided with initial breakup in Canada at *c.* 720 Ma<sup>6</sup>, and the  
38 Marinoan with a later phase of the same breakup event in Antarctica from  
39 670–650 Ma<sup>7</sup>. Another major breakup event between *c.* 615 Ma<sup>8</sup> and 550 Ma<sup>9</sup>  
40 formed the Iapetus Ocean (Fig. 1b), concurrent with the Gaskiers glaciation  
41 at *c.* 582–580 Ma.

42 It has been suggested that (a) continental breakup led to sharp increases in  
43 riverine runoff and silicate weathering (including flood basalts<sup>10</sup>), causing en-  
44 hanced  $\text{CO}_2$  drawdown and descent into a ‘snowball’ state<sup>4</sup>; and (b) deglacia-  
45 tion resulted from gradual accumulation of atmospheric  $\text{CO}_2$ <sup>11</sup>, likely from  
46 subaerial volcanic outgassing<sup>12</sup>, to critical levels capable of overcoming an ice  
47 albedo effect<sup>2</sup>. Intense debate centres on the source of alkalinity required to  
48 form the extensive cap carbonate sequences associated with Snowball Earth  
49 termination, and their negative  $\delta^{13}\text{C}$  signatures<sup>2,12,13</sup>. Carbonate sedimenta-  
50 tion may have occurred rapidly ( $<10$  kyr)<sup>12</sup> due to a post-glacial greenhouse  
51 weathering spike<sup>14,15</sup> of similar duration to Quaternary deglaciation<sup>16</sup>. How-  
52 ever, magnetopolarity reversals exhibited in some Marinoan cap carbonates  
53 suggest accumulation took place over longer timescales ( $\geq 100$  kyr)<sup>17,18</sup>. Sim-  
54 ilarly, meltback alone cannot easily explain the inferred increase in dissolved  
55 oceanic phosphate concentrations during the Tonian and Cryogenian peri-  
56 ods<sup>19</sup>. Despite the temporal coincidence between breakup of Rodinia and  
57 glaciations<sup>3,4</sup>, as yet no studies have investigated the direct impacts of vol-  
58 canism associated with extensive spreading ridge formation (Supplementary  
59 Information (SI) Fig. 1).

## 60 **The shallow ridge hypothesis**

61 Here we propose the novel shallow ridge hypothesis, which invokes ridge vol-  
62 canism to drive efficient and long-lived seafloor alteration, and in conjunction  
63 with other weathering processes linked to continental breakup<sup>4,10,20</sup> can rec-  
64 oncile many key features of Snowball Earth episodes.

65 Continental unzipping of the type associated with the breakup of Rodinia  
66 is accompanied by enhanced rifting and magmatism, and can coincide with  
67 an order of magnitude increase in magmatic productivity<sup>21</sup>. The early phase

68 of ocean crustal development involves a period of relatively shallow marine  
69 volcanism (Fig. 1c), as the ridge axis gradually subsides<sup>22</sup>. This low hydro-  
70 static pressure regime favours explosive fragmentation of lava in contact with  
71 seawater<sup>23</sup>, yielding voluminous hyaloclastite—a pyroclastic rock dominated  
72 by juvenile angular glass fragments—along the newly formed ridge (Fig. 1d).  
73 Hyaloclastite volcanism in early rifting environments is a rapid, high-volume  
74 process, forming from volcanic centres 30–40 km wide, and producing mounds  
75  $\sim 1.5$  km high and 15–20 km wide<sup>22</sup>. Observations and empirical subsidence  
76 relationships indicate that conditions favourable for hyaloclastite formation  
77 (depths up to 2 km) would persist along the ridge for at least 20 Myr (SI Fig.  
78 2).

79 The quenched glass shards typical of basaltic hyaloclastites are very suscep-  
80 tible to alteration, largely by hydration to palagonite<sup>24</sup>. This is enhanced by  
81 a high reactive surface area:volume ratio and high porosity (compared to pil-  
82 low lavas) that greatly increases seawater interaction. Basaltic glass alteration  
83 involves considerable element mobilisation (e.g. Ca losses of  $\sim 90\%$ <sup>25</sup>), thus  
84 has the potential to exert a major control on seawater chemistry<sup>24</sup>, including  
85 consumption of aqueous  $\text{CO}_2$ <sup>26</sup>. The shallow ridge is also a major source of  
86 magnesium, with basaltic glass experiencing Mg losses of  $\sim 67\%$ <sup>25</sup> to  $\sim 97\%$ <sup>24</sup>.  
87 Dissolution rates of basaltic glass could be reduced<sup>24</sup> at the low temperatures  
88 expected in an ice-covered ocean, but our model purely evaluates the initial  
89 element flux during rapid quenching, followed by cation leaching<sup>24</sup>, and does  
90 not require total glass dissolution. As hyaloclastites accumulate in thick ‘piles’  
91 along the ridge axis, they are susceptible to high temperature hydrothermal  
92 circulation leading to further losses through diffusion<sup>24</sup>—conditions thought  
93 to persist for  $\sim 10^6$  yr<sup>27</sup>. Conservatively, we only consider contributions from  
94 freshly erupted material close to the ridge axis. Palagonitization of basaltic  
95 glass occurs rapidly at high temperatures<sup>24</sup>, and potentially within one year  
96 in hydrothermal systems<sup>28</sup>. Thus, hyaloclastite alteration can be considered  
97 almost instantaneous on geological timescales.

98 This global scale process offers an alternative, complementary explanation for  
99 the surge of alkalinity associated with the Neoproterozoic “calcium ocean” and  
100 carbonate sedimentation, which cannot be satisfactorily explained by terres-  
101 trial weathering alone<sup>29</sup>. The process can also help explain the late Neopro-  
102 terozoic ‘excess phosphate ocean’<sup>19</sup> and high concentrations of  $\text{SiO}_2$  in banded  
103 iron formations (BIF)<sup>30</sup>. Although we focus on Rodinia, shallow ridge effects  
104 will have similarly large impacts on ocean fluxes during any major episode  
105 of continental breakup, albeit manifest in different ways due to variations in  
106 timescales and extent of magmatic productivity, alteration and biological pro-  
107 ductivity in the ocean. It is unclear why Pangea break-up did not result in  
108 global glaciation, although the more polar location of continents may have  
109 suppressed the continental silicate weathering  $\text{CO}_2$  sink.

## 110 Breakup of Rodinia

111 The 750–725 Ma breakup involved at least  $\sim 2 \times 10^4$  km spreading-ridge for-  
112 mation around the perimeter of Laurentia (Fig. 1a)<sup>3</sup>. Subsequent rift and  
113 drift episodes<sup>3,5</sup> may have increased the total length of new spreading ridges  
114 by 3–4 times. Although Neoproterozoic ocean crust is poorly represented in  
115 the geological record (e.g. due to subduction), there is evidence for widespread  
116 hyaloclastite emplacement during breakup, prior to ‘snowball’ glaciations (Fig.  
117 2). For example, the 717–716.5 Ma Mount Harper Volcanic Complex<sup>6</sup>—a 1.6  
118 km thick succession of subaqueous hyaloclastites, breccias and lavas emplaced  
119 along the rifted northwestern Laurentian margin<sup>31</sup>—is directly overlain by  
120 Sturtian glacial diamictites. Rift-related volcanism would have continued dur-  
121 ing glaciations (SI Table 1), as newly formed ocean crust progressively un-  
122 zipped to form the extensive Proto-Pacific ridge system. Crucially, and in con-  
123 trast to most other biogeochemical fluxes, hyaloclastite-derived ocean fluxes  
124 will not have been affected by near-global ice cover.

125 There is also evidence for extensive volcanism, again associated with Rodinia  
126 breakup, prior to the Marinoan glaciation (e.g. 670–650 Ma in Antarctica<sup>7</sup>;  
127 Fig. 2). The apparent ‘delay’ in initiation of rifting between Laurentia and  
128 Antarctica confirms that breakup was protracted<sup>3</sup>, and seafloor spreading con-  
129 tinued throughout the Sturtian and Marinoan glaciations. Similarly, basaltic  
130 hyaloclastites associated with the early opening of Iapetus ( $\sim 615$ –580 Ma) are  
131 recognised globally (Fig. 2; SI Table 1). Hyaloclastites are directly overlain  
132 by diamictites associated with the Gaskiers glaciation<sup>32</sup>, signifying explosive  
133 shallow marine volcanism before (and likely during) the Gaskiers event (Fig.  
134 2).

135 Better time constraints in the Neoproterozoic are needed to explore whether  
136 shallow ridge volcanism could have played a key role in initiating snowball  
137 glaciation. However, this is feasible given: (1) an intrinsic need for continental  
138 breakup in order to intensify silicate weathering<sup>4,10</sup>, and (2) isotopic evidence  
139 for copious weathering of juvenile mantle-derived volcanics before the Sturtian  
140 glaciation<sup>33</sup>.

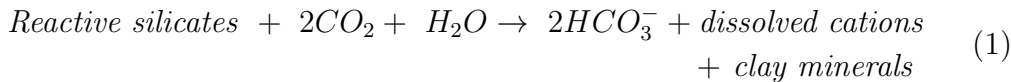
## 141 Hyaloclastite alteration fluxes into the ocean

142 We develop Monte Carlo simulations to quantify potential chemical fluxes (Ca,  
143 P, Si, Mg) into the ocean during shallow ridge volcanism. Given the significant  
144 uncertainties in initial conditions and fluxes (e.g. seawater chemistry, pH), this  
145 situation does not lend itself to deterministic modelling, but instead must be  
146 probabilistically assessed. Here, we present a parsimonious model, supported

147 by observations and experiments (Table 1, methods), broadly capturing the  
 148 key processes and associated uncertainties. Ridge length is varied from 0.5 to 2  
 149  $\times 10^4$  km to simulate progressive separation of Laurentia<sup>3</sup>, and full spreading  
 150 rates from 50 to 200 mm yr<sup>-1</sup> to represent moderate<sup>34</sup> to fast<sup>35</sup> rates expected  
 151 during breakup<sup>5</sup>. The simulations account for secondary mineral formation,  
 152 for example carbonate fluorapatite (CFA) formation following release of P<sub>2</sub>O<sub>5</sub>  
 153 during glass alteration, and smectite (saponite) formation as a sink for silica.  
 154 Fluxes calculated here exclude background seafloor weathering and hydrother-  
 155 mal processes<sup>36</sup> associated with contemporary deep ridge systems, e.g. in the  
 156 Mirovia superocean (Fig. 1a), which would increase Ca, P, Si and Mg oceanic  
 157 input.

158 Hyaloclastite formation rates (and hence magnitude of the chemical fluxes)  
 159 vary spatially and temporally during ridge formation, hence our deliberately  
 160 wide and conservative parameter ranges (Table 1). All input distributions are  
 161 sampled independently because of insufficient observational evidence to ac-  
 162 curately define correlations, but three more tightly constrained scenarios (SI  
 163 Table 2) explore sensitivity of the calculated fluxes to independence assump-  
 164 tions. The high hyaloclastite production scenario (I, SI Table 2) involves both  
 165 rapid and spatially extensive unzipping. A further simulation explores the po-  
 166 tential correlation between ridge length and magmatic productivity, arising  
 167 from the temporal evolution of the ridge system.

168 Given CaO losses from hyaloclastites range from 4–10 wt%<sup>24,25</sup>, our simu-  
 169 lations suggest optimal spreading conditions along the length of the Proto-  
 170 Pacific ridge could yield a maximum Ca flux of  $1.4 \times 10^{13}$  mol yr<sup>-1</sup> (Fig. 3a;  
 171 SI Fig. 3a); comparable to the modern dissolved riverine flux of  $\sim 1.2 \times 10^{13}$   
 172 mol yr<sup>-1</sup> (ref.<sup>37</sup>) and 1–3 orders of magnitude greater than the modern hy-  
 173 drothermal ridge flux ( $9\text{--}1300 \times 10^9$  mol yr<sup>-1</sup>)<sup>38</sup>. Glass alteration also results  
 174 in uptake of CO<sub>2</sub> from solution<sup>39</sup> according to the approximate reaction:



175 Ca forms most of the charge balance carried by the dissolved cation budget  
 176 released to solution during glass alteration. Mg and Na contribute most of  
 177 the remainder, along with a small uptake of K<sup>24</sup>. Thus, a combined Ca, Mg  
 178 and Na (-K) flux of approximately  $2 \times 10^{13}$  mol yr<sup>-1</sup> during hyaloclastite  
 179 alteration results in uptake of  $4 \times 10^{13}$  mol yr<sup>-1</sup> of CO<sub>2</sub>. By comparison, the  
 180 global rate of continental silicate weathering is  $1.2 \times 10^{13}$  mol yr<sup>-1</sup> of CO<sub>2</sub>  
 181 (ref.<sup>40</sup>).

182 Hyaloclastite alteration in an ice-covered ocean provides a major source of  
 183 alkalinity—additional to that provided by the long-term alteration of the  
 184 oceanic crust<sup>20</sup>—driving up carbonate production immediately after Snowball  
 185 Earth glaciations. The cap carbonate sequences that formed globally on con-

186 tinal margins, typically overlying glacial diamictites<sup>2,12</sup>, are commonly at-  
187 tributed to enhanced terrestrial weathering of carbonate-rich sediments during  
188 and after glaciation<sup>14,15</sup>. However, to achieve observed cap carbonate thick-  
189 nesses (some >100 m, Figs 3c,d) would require extreme levels of terrestrial  
190 weathering, delivering  $\sim 10^2$ – $10^3$  times the present annual supply of dissolved  
191 cations to the oceans<sup>29</sup>. Continental runoff during the post-snowball green-  
192 house ( $400\times$  modern  $p\text{CO}_2$ ) likely produced  $\sim 1.2$  times the modern riverine  
193 runoff<sup>16</sup>, suggesting subaerial weathering alone cannot explain cap carbonate  
194 production<sup>29</sup>.

195 We propose that under near-global ice cover, which suppresses normal removal  
196 processes, a prolonged state of hyaloclastite eruption and alteration would su-  
197 persaturate seawater with  $\text{Ca}^{2+}$  and  $\text{Mg}^{2+}$ . This is consistent with evidence  
198 for rapid carbonate sedimentation (spontaneous nucleation) following glacia-  
199 tions<sup>2,12,15</sup>. The question is whether requisite degrees of supersaturation are  
200 feasible over such prolonged timescales (order 10 Myr). At our maximum esti-  
201 mated discharge rate (the trivial case with no initial dissolved  $\text{Ca}^{2+}$  or  $\text{Mg}^{2+}$ )  
202 the ocean reaches saturation within 1–3 Myr ( $\text{Ca}^{2+}$  and  $\text{Mg}^{2+}$ , respectively).  
203 A 10 Myr glaciation could therefore yield degrees of supersaturation exceed-  
204 ing  $12\times$  ( $\text{Ca}^{2+}$ ) and  $3\times$  ( $\text{Mg}^{2+}$ ), certainly feasible in the light of observa-  
205 tions of experimental solutions<sup>41</sup>, geological fluids<sup>42</sup>, and the present-day sur-  
206 face ocean<sup>43</sup>. In the glacial aftermath, conditions become more favourable for  
207 rapid precipitation: higher ocean temperatures, renewed photosynthesis, in-  
208 creased primary productivity, enhanced atmospheric  $\text{CO}_2$  exchange, and im-  
209 portantly, resumption of particle settling providing carbonate condensation  
210 nuclei. Volcanism before and after glaciations (Fig. 2; SI Table 1) will also  
211 have contributed to carbonate deposition, although in the absence of ice cover  
212 (limiting build-up in the ocean) would occur more gradually. Combined with  
213 the rate-limiting influence of platform subsidence<sup>2</sup>, this may explain slower  
214 sedimentation rates inferred for some Marinoan carbonate sequences<sup>17,18</sup>.

215 In an ice-covered ocean, limited atmospheric exchange leads to rapid conver-  
216 sion of dissolved  $\text{CO}_2$  to bicarbonate ( $\text{HCO}_3^-$ , which constitutes the majority  
217 of seawater DIC) by equation [1]. However, hyaloclastite formation is also asso-  
218 ciated with  $\text{CO}_2$  degassing from erupted basalt, particularly at shallow depths.  
219 Assuming a pre-eruptive  $\text{CO}_2$  concentration of 0.5 wt% in the basalts and total  
220 degassing, hyaloclastite emplacement could release  $\sim 0.03$ – $1.3 \times 10^{12}$  mol  $\text{yr}^{-1}$   
221  $\text{CO}_2$ , broadly consistent with the ridge flux ( $\sim 0.8 \times 10^{12}$  mol  $\text{yr}^{-1}$ ) assumed  
222 for the ‘snowball’ ocean<sup>2</sup>. This is not a completely closed system: cracks in sea-  
223 ice<sup>44</sup> will have permitted some  $\text{CO}_2$  outgassing. Equally, ice-free regions will  
224 have allowed  $\text{CO}_2$  ingassing during a period when atmospheric  $\text{CO}_2$  levels due  
225 to subaerial volcanism<sup>2</sup> ultimately exceeded present-day levels by two to three  
226 orders of magnitude<sup>11</sup>, a net  $\text{CO}_2$  gain. The long-term  $\text{CO}_2$  input from volcan-  
227 ism and hydrothermal activity can explain mantle-like  $\delta^{13}\text{C}$  signatures ( $-6 \pm$   
228  $1\%$ ) observed in many cap carbonates<sup>2,12,13</sup>. Stratigraphic or localised carbon-

229 ate  $\delta^{13}\text{C}$  increases<sup>29</sup> may reflect increases in biological productivity, organic  
230 carbon burial, and intensified subaerial carbonate weathering—all expected in  
231 the snowball aftermath<sup>15,19</sup>.

232 Some post-Sturtian cap carbonates exhibit  $^{187}\text{Os}/^{188}\text{Os}$  ratios consistent with  
233 continental inputs<sup>33</sup>, again expected during a post-glacial weathering spike.  
234 However, many cap carbonates exhibit only minor shifts in  $^{87}\text{Sr}/^{86}\text{Sr}$  (refs. <sup>15,29</sup>),  
235 suggesting that enhanced terrestrial weathering was not dominant in their  
236 production<sup>29</sup>. Pre-Marinoan carbonates (800–650 Ma) exhibit relatively low  
237  $^{87}\text{Sr}/^{86}\text{Sr}$  (ref. <sup>45</sup>), compatible with significant hydrothermal ridge contribu-  
238 tions<sup>46</sup>, which will progressively dominate the Sr isotope inventory in seawater  
239 under ice cover with much reduced continental runoff<sup>15</sup>. Further, widespread  
240 enrichment of heavy rare earth elements (REE) and positive Eu and Y anom-  
241 alies in Sturtian<sup>47</sup> and Marinoan<sup>48</sup> cap carbonates can be explained by alter-  
242 ation of mid-ocean ridge basalts and wholesale mixing of hydrothermal fluids  
243 in the ocean<sup>48,49</sup>.

244 The maximum simulated  $\text{Ca}^{2+}$  flux (Fig. 3a) would yield  $\sim 18.5$  m-thick build-  
245 up (mean estimate 2 m, median 1.2 m, Fig. 3c) of carbonate over an area  
246 equivalent to the present-day continental shelf for every  $10^6$  years of ridge  
247 formation. Given the Sturtian (diachronous<sup>50</sup>) and Marinoan glaciations per-  
248 sisted for  $\sim 55$  Myr<sup>33</sup> and  $\sim 12$  Myr<sup>51</sup>, respectively, these accumulations are of  
249 the same order as observed cap carbonates, typically metres to tens of metres  
250 thick<sup>12</sup> (Fig. 3c).

251 Ridge alteration could produce magnesium fluxes of the order  $1\text{--}6 \times 10^{12}$  mol  
252  $\text{yr}^{-1}$  (Fig. 3b and SI Table 2; modern riverine Mg flux is  $5.1 \times 10^{12}$  mol  $\text{yr}^{-1}$ )<sup>37</sup>,  
253 potentially contributing  $\sim 2\text{--}15$  m-thick dolostone for every  $10^6$  years of ridge  
254 formation. Accordingly, our model suggests the Marinoan event could yield  
255  $20\text{--}150$  m-thick dolostone, consistent with observed global mean and maxi-  
256 mum thicknesses of 18.5 m and 175 m respectively<sup>52</sup> (Fig. 3d). On timescales  
257 typically associated with deglaciation (c. 10 kyr), continental weathering is  
258 only likely to supply enough  $\text{Mg}^{2+}$  to produce a  $\sim 0.5$  m thick cap dolostone<sup>16</sup>.  
259 Therefore our hypothesis provides an important or even dominant additional  
260 source of  $\text{Ca}^{2+}$  and  $\text{Mg}^{2+}$ , and can help explain not only the qualitative associ-  
261 ation of cap carbonate and dolostone sequences with Snowball Earth episodes,  
262 but also observed thicknesses of these deposits.

263 Although up to 90%  $\text{P}_2\text{O}_5$  in fresh basaltic glass can be released during alter-  
264 ation<sup>25</sup>, we assume a conservative 20–80% loss, based on modern palagonites<sup>24</sup>.  
265 Simulations show that high spreading rates ( $>100$  mm  $\text{yr}^{-1}$ ) coupled with ex-  
266 tensive ridges ( $>15 \times 10^3$  km), could yield dissolved phosphorus fluxes up to  
267  $7 \times 10^{11}$  mol  $\text{yr}^{-1}$  (Fig. 4a; SI Fig. 3b), roughly 20 times the modern dissolved  
268 riverine flux ( $3.1 \times 10^{10}$  mol  $\text{yr}^{-1}$ )<sup>37</sup>. For the full simulation (SI Table 2), the  
269 median phosphorus flux ( $3.7 \times 10^{10}$  mol  $\text{yr}^{-1}$ ) is comparable to the modern



270 riverine contribution, and the high hyaloclastite production scenario yields a  
271 flux  $\sim 7$  times greater ( $2.3 \times 10^{11}$  mol yr<sup>-1</sup>; Fig. 4b). Assuming full unzipping  
272 and substantial secondary mineralisation losses (SI Fig. 4), there is  $\sim 70\%$   
273 probability that P-influx would exceed the modern riverine flux (SI Fig. 5).  
274 In the modern ocean, phosphate sorption onto ferric oxyhydroxides represents  
275 a significant sink, but this is thought to have been of minor importance in  
276 the Neoproterozoic due to high oceanic silicic acid concentrations—as silica  
277 hydroxides suppress phosphate sorption onto ferric oxyhydroxides<sup>19</sup>.

278 Hyaloclastite alteration during ridge unzipping provides a viable mechanism to  
279 account for anomalously high seawater phosphorus levels (5–10 times Phanero-  
280 zoic levels, according to P:Fe ratios in sedimentary iron formations)<sup>19</sup> in-  
281 ferred for Snowball Earth episodes. This ‘excess phosphate ocean’ has been  
282 attributed to enhanced weathering of glacial deposits during the ‘snowball’  
283 thaw phase<sup>19</sup>. Although relevant, post-glacial weathering would be expected  
284 to yield a relatively short-lived ( $\sim 10$ – $100$  kyr)<sup>16</sup> increase in phosphate, and  
285 could be problematic in view of the low solubility of apatite. Our model pro-  
286 vides a mechanism for producing high dissolved phosphorus levels that, in the  
287 absence of biological removal, could persist over  $\sim 10$ – $100$  Myr (Fig. 2), over  
288 repeated cycles (i.e., protracted opening of the Proto-Pacific followed by Iape-  
289 tus in Ediacaran times; Fig. 1b)<sup>3</sup>. This process operated independently, and in  
290 addition to other mechanisms, such as biotic enhancement of apatite weath-  
291 ering linked to increased weathering rates via microbial colonisation of the  
292 land<sup>53</sup>, and subaerial weathering of large igneous provinces<sup>54</sup> (notably during  
293 the Tonian period; Fig. 2).

294 The shallow ridge can also contribute to relatively high dissolved oceanic sili-  
295 cic acid concentrations inferred for the Neoproterozoic<sup>19</sup>, and the SiO<sub>2</sub>-rich  
296 ( $\sim 30$ – $55\%$ ) banded iron formations (BIF) that served as a (local) silica sink  
297 during the Sturtian<sup>30,55</sup>, and possibly, but not ostensibly, during the Mari-  
298 noan<sup>55</sup> glaciations. Basaltic glass alteration results in loss of an average  $\sim 16$   
299 wt% SiO<sub>2</sub><sup>24</sup> (potentially up to  $50\%$ )<sup>25</sup>, thus contributing up to  $10\times$  the current  
300 riverine flux of  $\sim 6.4 \times 10^{12}$  mol yr<sup>-1</sup> (ref.<sup>37</sup>) to the ocean during extensive  
301 hyaloclastite alteration (SI Table 2, SI Fig. 6b). High hydrothermal Fe fluxes<sup>48</sup>  
302 are expected in our low hydrostatic pressure regime<sup>56</sup>, and a dominance of hy-  
303 drothermal inputs is supported by mantle-like Nd and Pb isotope signatures  
304 observed in some BIFs<sup>30</sup>. Thus, our hypothesis might help elucidate the com-  
305 mon association between BIFs and mafic volcanics<sup>55</sup>, although this requires  
306 further validation, particularly given the localised nature of many BIFs.

## 307 Consequences of a shallow ridge system

308 The discovery that Earth experienced near-total ice cover for prolonged peri-  
309 ods in the Neoproterozoic has greatly enhanced understanding of Earth his-  
310 tory, but critical aspects remain unresolved. We demonstrate how enhanced  
311 shallow marine volcanic activity, persisting for >20 Myr in the absence of most  
312 biological removal processes, would have driven major changes in ocean chem-  
313 istry. Our shallow ridge hypothesis advances understanding of Snowball Earth  
314 events, qualitatively and quantitatively explaining many enigmatic features  
315 including: increased ocean alkalinity;  $^{13}\text{C}$ -depleted cap carbonate sequences;  
316 and high silica concentrations manifest in banded iron formations.

317 Our hypothesis provides a critical quantitative explanation for unusually high  
318 dissolved phosphate inputs to late Proterozoic oceans. This enhanced supply  
319 likely drove the increase in primary productivity required to generate the large  
320 rise in atmospheric oxygen levels that occurred in the wake of Snowball Earth  
321 events<sup>19</sup>. We infer that shallow ridge volcanism associated with the Proto-  
322 Pacific and Iapetan rifts also prompted oxidation of the Ediacaran ocean<sup>57</sup>,  
323 which would have facilitated the emergence of multicellular life.

## 324 Methods

325 Methods and any associated references are available in the online version of  
326 the paper.

## 327 References

- 328 1. Kirschvink, J. L. Late Proterozoic low latitude glaciation: The Snowball  
329 Earth. In *The Proterozoic Biosphere: A Multidisciplinary Study*, Schopf,  
330 J. W. and Klein, C., editors, 51–52. Cambridge Univ. Press, New York  
331 (1992).
- 332 2. Hoffman, P. F., Kaufman, A. J., Halverson, G. P., and Schrag, D. P. A  
333 Neoproterozoic Snowball Earth. *Science* **281**, 1342–1346 (1998).
- 334 3. Eyles, N. and Januszczak, N. ‘Zipper-rift’: a tectonic model for Neopro-  
335 terozoic glaciations during the breakup of Rodinia after 750 Ma. *Earth-*  
336 *Science Reviews* **65**, 1–73 (2004).
- 337 4. Donnadieu, Y., Godderis, Y., Ramstein, G., Nedelec, A., and Meert, J.  
338 A ‘snowball earth’ climate triggered by continental break-up through  
339 changes in runoff. *Nature* **428**, 303–306 (2004).
- 340 5. Torsvik, T. H., Smethurst, M. A., Meert, J. G., Van der Voo, R., McK-  
341 errow, W. S., Brasier, M. D., Sturt, B. A., and Walderhaug, H. J. Con-

- 342 tinenta break-up and collision in the Neoproterozoic and Palaeozoic —A  
343 tale of Baltica and Laurentia. *Earth-Science Reviews* **40**, 229–258 (1996).
- 344 6. Macdonald, F. A., Schmitz, M. D., Crowley, J. L., Roots, C. F., Jones,  
345 D. S., Maloof, A. C., Strauss, J. V., Cohen, P. A., Johnston, D. T., and  
346 Schrag, D. P. Calibrating the Cryogenian. *Science* **327**, 1241–1243, 03  
347 (2010).
- 348 7. Cooper, A. F., Maas, R., Scott, J. M., and Barber, A. J. W. Dating of  
349 volcanism and sedimentation in the Skelton Group, Transantarctic Moun-  
350 tains: Implications for the Rodinia-Gondwana transition in southern Vic-  
351 toria Land, Antarctica. *Geological Society of America Bulletin* **123**, 681–  
352 702 (2011).
- 353 8. O’Brien, T. M. and van der Pluijm, B. A. Timing of Iapetus Ocean rifting  
354 from Ar geochronology of pseudotachylytes in the St. Lawrence rift system  
355 of southern Quebec. *Geology* **40**, 443–446 (2012).
- 356 9. Van Staal, C. R., Dewey, J. F., MacNiocail, C., and McKerrow, W. S.  
357 The Cambrian-Silurian tectonic evolution of the northern Appalachians  
358 and British Caledonides: history of a complex, west and southwest Pacific-  
359 type segment of Iapetus. *Geological Society, London, Special Publications*  
360 **143**, 197–242 (1998).
- 361 10. Godd ris, Y., Donnadiou, Y., N d lec, A., Dupr , B., Dessert, C., Gard,  
362 A., Ramstein, G., and Fran ois, L. M. The Sturtian ‘snowball’ glaciation:  
363 fire and ice. *Earth and Planetary Science Letters* **211**, 1–12 (2003).
- 364 11. Pierrehumbert, R. T. High levels of atmospheric carbon dioxide necessary  
365 for the termination of global glaciation. *Nature* **429**, 646–649 (2004).
- 366 12. Hoffman, P. F. and Schrag, D. P. The snowball Earth hypothesis: testing  
367 the limits of global change. *Terra Nova* **14**, 129–155 (2002).
- 368 13. Halverson, G. P. and Shields-Zhou, G. Chapter 4 Chemostratigraphy  
369 and the Neoproterozoic glaciations. *Geological Society, London, Memoirs*  
370 **36**(1), 51–66 (2011).
- 371 14. Fairchild, I. J. Balmy Shores and Icy Wastes: The Paradox of Carbonates  
372 Associated with Glacial Deposits in Neoproterozoic Times. *Sedimentology*  
373 *Review* **1**, 1–16 (1993).
- 374 15. Higgins, J. A. and Schrag, D. P. Aftermath of a snowball Earth. *Geo-*  
375 *chemistry, Geophysics, Geosystems* **4**, 1028 (2003).
- 376 16. Le Hir, G., Donnadiou, Y., Godd ris, Y., Pierrehumbert, R. T., Halverson,  
377 G. P., Macouin, M., N d lec, A., and Ramstein, G. The snowball Earth  
378 aftermath: Exploring the limits of continental weathering processes. *Earth*  
379 *and Planetary Science Letters* **277**, 453–463 (2009).
- 380 17. Trindade, R. I. F., Font, E., D’Agrella-Filho, M. S., Nogueira, A. C. R.,  
381 and Riccomini, C. Low-latitude and multiple geomagnetic reversals in  
382 the Neoproterozoic Puga cap carbonate, Amazon craton. *Terra Nova* **15**,  
383 441–446 (2003).
- 384 18. Kennedy, M. J. and Christie-Blick, N. Condensation origin for Neopro-  
385 terozoic cap carbonates during deglaciation. *Geology* **39**, 319–322 (2011).
- 386 19. Planavsky, N. J., Rouxel, O. J., Bekker, A., Lalonde, S. V., Konhauser,

- 387 K. O., Reinhard, C. T., and Lyons, T. W. The evolution of the marine  
388 phosphate reservoir. *Nature* **467**, 1088–1090 (2010).
- 389 20. Le Hir, G., Ramstein, G., Donnadieu, Y., and Godd eris, Y. Scenario for  
390 the evolution of atmospheric pCO<sub>2</sub> during a snowball Earth. *Geology* **36**,  
391 47–50 (2008).
- 392 21. Storey, M., Duncan, R. A., and Tegner, C. Timing and duration of volcan-  
393 ism in the North Atlantic Igneous Province: Implications for geodynamics  
394 and links to the Iceland hotspot. *Chemical Geology* **241**, 264–281 (2007).
- 395 22. Planke, S., Symonds, P. A., Alvestad, E., and Skogseid, J. Seismic vol-  
396 canostratigraphy of large-volume basaltic extrusive complexes on rifted  
397 margins. *Journal of Geophysical Research* **105**, 19335–19351. (2000).
- 398 23. Batiza, R. and White, J. D. L. Submarine lavas and hyaloclastite. In En-  
399 cyclopedia of Volcanoes, Sigurdsson, H., editor, 361–381. Academic Press,  
400 San Diego (2000).
- 401 24. Stroncik, N. A. and Schmincke, H. U. Palagonite – a review. *International*  
402 *Journal of Earth Sciences* **91**, 680–697 (2002).
- 403 25. Staudigel, H. and Hart, S. R. Alteration of basaltic glass: mechanisms  
404 and significance for the oceanic crust-sea water budget. *Geochimica et*  
405 *Cosmochimica Acta* **47**, 337–350 (1983).
- 406 26. Brady, P. V. and G islas on, S. R. Seafloor weathering controls on atmo-  
407 spheric CO<sub>2</sub> and global climate. *Geochimica et Cosmochimica Acta* **61**,  
408 965–973 (1987).
- 409 27. Mottl, M. J. and Wheat, C. G. Hydrothermal circulation through mid-  
410 ocean ridge flanks: Fluxes of heat and magnesium. *Geochimica et Cos-*  
411 *mochimica Acta* **58**, 2225–2237 (1994).
- 412 28. Jakobsson, S. P. Environmental factors controlling the palagonitization  
413 of the tephra of the Surtsey volcanic island, Iceland. *Bull. Geol. Soc.*  
414 *Denmark* **27**, 91–105 (1978).
- 415 29. Kennedy, M. J., Christie-Blick, N., and Prave, A. R. Carbon isotopic  
416 composition of Neoproterozoic glacial carbonates as a test of paleocean-  
417 ographic models for snowball Earth phenomena. *Geology* **29**, 1135–1138  
418 (2001).
- 419 30. Stern, R. J., Mukherjee, S. K., Miller, N. R., Ali, K., and Johnson,  
420 P. R. ~750 Ma banded iron formation from the Arabian-Nubian Shield—  
421 Implications for understanding neoproterozoic tectonics, volcanism, and  
422 climate change. *Precambrian Research* **239**, 79–94 (2013).
- 423 31. Cox, G. M., Roots, C. F., Halverson, G. P., Minarik, W. G., Macdonald,  
424 F. A., and Hubert-Theou, L. Mount Harper Volcanic Complex, Ogilvie  
425 Mountains: A far-flung occurrence of the Franklin Igneous Event. In Yukon  
426 Exploration and Geology 2012, MacFarlane, K. E., Nordling, M. G., and  
427 Sack, P. J., editors, 19–36. Yukon Geological Survey (2013).
- 428 32. Calver, C. R., Black, L. P., Everard, J. L., and Seymour, D. B. U-Pb zircon  
429 age constraints on late Neoproterozoic glaciation in Tasmania. *Geology* **32**,  
430 893–896 (2004).
- 431 33. Rooney, A. D., Macdonald, F. A., Strauss, J. V., Dud as, F.  ., Hall-

- 432 mann, C., and Selby, D. Re-Os geochronology and coupled Os-Sr isotope  
433 constraints on the Sturtian snowball Earth. *Proceedings of the National*  
434 *Academy of Sciences* **111**, 51–56 (2014).
- 435 34. Reid, I. and Jackson, H. R. Oceanic spreading rate and crustal thickness.  
436 *Marine Geophysical Researches* **5**, 165–172 (1981).
- 437 35. Wilson, D. S. Fastest known spreading on the Miocene Cocos-Pacific Plate  
438 Boundary. *Geophysical Research Letters* **23**, 3003–3006 (1996).
- 439 36. Alt, J. C. Subseafloor Processes in Mid-Ocean Ridge Hydrothermal Sys-  
440 tems. In *Seafloor Hydrothermal Systems: Physical, Chemical, Biolog-  
441 ical, and Geological Interactions*, Humphris, S. E., Zierenberg, R. A.,  
442 Mullineaux, L. S., and Thomson, R. E., editors, number 91, 85–114. Amer-  
443 ican Geophysical Union (1995).
- 444 37. Berner, E. K. and Berner, R. A. *Global Environment: Water, Air, and*  
445 *Geochemical Cycles*. Princeton University Press, 2 edition, (2012).
- 446 38. Elderfield, H. and Schultz, A. Mid-ocean ridge hydrothermal fluxes and the  
447 chemical composition of the ocean. *Annual Review of Earth and Planetary*  
448 *Sciences* **24**, 191–224 (1996).
- 449 39. Wallmann, K., Aloisi, G., Haeckel, M., Tishchenko, P., Pavlova, G., Grein-  
450 ert, J., Kutterolf, S., and Eisenhauer, A. Silicate weathering in anoxic ma-  
451 rine sediments. *Geochimica et Cosmochimica Acta* **72**, 2895–2918 (2008).
- 452 40. Gaillardet, J., Dupré, B., Louvat, P., and Allègre, C. J. Global silicate  
453 weathering and CO<sub>2</sub> consumption rates deduced from the chemistry of  
454 large rivers. *Chemical Geology* **159**, 3–30 (1999).
- 455 41. Pokrovsky, O. Precipitation of calcium and magnesium carbonates from  
456 homogeneous supersaturated solutions. *Journal of Crystal Growth* **186**,  
457 233 – 239 (1998).
- 458 42. Compton, J. S. Degree of supersaturation and precipitation of organogenic  
459 dolomite. *Geology* **16**, 318–321 (1988).
- 460 43. Pokrovsky, O. S. Kinetics of CaCO<sub>3</sub> homogeneous precipitation in seawa-  
461 ter. *Mineralogical Magazine* **58A**, 738–739 (1994).
- 462 44. Allen, P. A. and Etienne, J. L. Sedimentary challenge to Snowball Earth.  
463 *Nature Geosci* **1**, 817–825 (2008).
- 464 45. Kaufman, A. J., Jacobsen, S. B., and Knoll, A. H. The Vendian record  
465 of Sr and C isotopic variations in seawater: Implications for tectonics and  
466 paleoclimate. *Earth and Planetary Science Letters* **120**, 409–430 (1993).
- 467 46. Halverson, G. P., Dudás, F. Ö., Maloof, A. C., and Bowring, S. A. Evo-  
468 lution of the <sup>87</sup>Sr/<sup>86</sup>Sr composition of Neoproterozoic seawater. *Palaeo-*  
469 *geography, Palaeoclimatology, Palaeoecology* **256**, 103–129 (2007).
- 470 47. Meyer, E. E., Quicksall, A. N., Landis, J. D., Link, P. K., and Bostick,  
471 B. C. Trace and rare earth elemental investigation of a Sturtian cap  
472 carbonate, Pocatello, Idaho: Evidence for ocean redox conditions before  
473 and during carbonate deposition. *Precambrian Research* **192–195**, 89–106  
474 (2012).
- 475 48. Huang, J., Chu, X., Jiang, G., Feng, L., and Chang, H. Hydrothermal  
476 origin of elevated iron, manganese and redox-sensitive trace elements in

- 477 the c. 635 Ma Doushantuo cap carbonate. *Journal of the Geological Society*  
478 **168**, 805–816 (2011).
- 479 49. Young, G. M. Precambrian supercontinents, glaciations, atmospheric oxy-  
480 genation, metazoan evolution and an impact that may have changed the  
481 second half of Earth history. *Geoscience Frontiers* **4**, 247–261 (2013).
- 482 50. Kendall, B., Creaser, R. A., and Selby, D. Re-Os geochronology of post-  
483 glacial black shales in Australia: Constraints on the timing of “Sturtian”  
484 glaciation. *Geology* **34**, 729–732 (2006).
- 485 51. Bodisilitsch, B., Koeberl, C., Master, S., and Reimold, W. U. Estimatin-  
486 ing duration and intensity of Neoproterozoic snowball glaciations from Ir  
487 anomalies. *Science* **308**, 239–242 (2005).
- 488 52. Hoffman, P. F., Halverson, G. P., Domack, E. W., Husson, J. M., Higgins,  
489 J. A., and Schrag, D. P. Are basal Ediacaran (635 Ma) post-glacial “cap  
490 dolostones” diachronous? *Earth and Planetary Science Letters* **258**, 114–  
491 131 (2007).
- 492 53. Lenton, T. M. and Watson, A. J. Biotic enhancement of weathering, at-  
493 mospheric oxygen and carbon dioxide in the Neoproterozoic. *Geophysical*  
494 *Research Letters* **31**, L05202 (2004).
- 495 54. Horton, F. Did phosphorus derived from the weathering of large igneous  
496 provinces fertilize the Neoproterozoic ocean? *Geochemistry, Geophysics,*  
497 *Geosystems* **16**, 1723–1738 (2015).
- 498 55. Cox, G. M., Halverson, G. P., Minarik, W. G., Heron, D. P. L., Macdonald,  
499 F. A., Bellefroid, E. J., and Strauss, J. V. Neoproterozoic iron formation:  
500 An evaluation of its temporal, environmental and tectonic significance.  
501 *Chemical Geology* **362**, 232 – 249 (2013).
- 502 56. Kump, L. R. and Seyfried Jr., W. E. Hydrothermal Fe fluxes during  
503 the Precambrian: Effect of low oceanic sulfate concentrations and low  
504 hydrostatic pressure on the composition of black smokers. *Earth and*  
505 *Planetary Science Letters* **235**, 654–662 (2005).
- 506 57. Fike, D. A., Grotzinger, J. P., Pratt, L. M., and Summons, R. E. Oxidation  
507 of the Ediacaran Ocean. *Nature* **444**, 744–747 (2006).

## 508 Acknowledgements

509 E.J.R. acknowledges Australian Research Council Laureate Fellowship FL1201  
510 00050. We are grateful to R.S.J. Sparks, R.N. Taylor, C.N. Trueman, T.  
511 Lenton, I. Fairchild and G. Shields-Zhou for helpful discussions and sugges-  
512 tions. Supplementary Information figure 1 was illustrated by Gary Hincks.

513 **Author contributions**

514 The research was conceived and managed by T.G. T.H. developed and per-  
515 formed simulations with inputs from T.G., T.T., M.R.P. and E.J.R. The  
516 manuscript was written by T.G. with important contributions from all co-  
517 authors.

518 **Additional information**

519 Supplementary information is available in the online version of the paper.  
520 Reprints and permission information is available online at [www.nature.com/](http://www.nature.com/reprints)  
521 reprints. Correspondence and requests for materials should be addressed to  
522 T.G.

523 **Competing financial interests**

524 The authors declare no competing financial interests.

525 **Figure captions**

526 **Figure 1 | Evolution of spreading ridge systems during the late Neo-**  
527 **proterozoic. a.** Continental reconstructions at  $\sim 750$  Ma showing location of  
528 the Proto-Pacific rift system, and **b,** at  $\sim 600$  Ma showing inferred location  
529 of the Iapetan rift (modified after ref.<sup>10</sup>). **c.** During the early phase of plume  
530 magmatism ( $\sim 800$  Ma), volcanism was largely subaerial (Supplementary In-  
531 formation Table 1); however, as rifting occurred, the main axis of volcanism  
532 submerged below sea-level resulting in the formation of the Proto-Pacific (and  
533 Iapetus at  $\sim 600$  Ma) and a sustained phase of shallow marine volcanism.  
534 **d.** Under these conditions (shown here prior to glaciation), hyaloclastites are  
535 formed preferentially by quenching and explosive shattering of lava in contact  
536 with seawater, forming ‘fresh’ highly alterable glasses.

537 **Figure 2 | Summary of major global volcanic events during the To-**  
538 **nian, Cryogenian and early Ediacaran periods, in relation to major**  
539 **glaciations (blue) and continental breakup events (beige).** Red bars  
540 signify major volcanic events involving extensive hyaloclastite emplacement  
541 (see Supplementary Information Table 1 for more information); note LIP:  
542 Large Igneous Province; ANS: Arabian-Nubian Shield.

543 **Figure 3 | Monte Carlo simulations showing estimated Ca and Mg**  
544 **fluxes into the ‘snowball’ ocean, and resulting thicknesses of car-**  
545 **bonate and dolostone.** Input parameter ranges are defined in Table 1. Note  
546 the logarithmic scales for the flux axes in (a) and (b). **a.** Flux of Ca, ac-  
547 counting for a variable percentage lost to  $\text{CaCO}_3$  cementation. **b.** Flux of Mg,  
548 accounting for in situ dolomite cementation; lines denote the modern annual  
549 riverine dissolved Ca and Mg fluxes for comparison. Note that **(a)** and **(b)**  
550 represent the full simulation (SI Table 2). **c.** & **d.** Probability of exceedance  
551 for cap carbonate **(c)** and dolostone **(d)** thicknesses resulting from accumu-  
552 lation of Ca and Mg, respectively, in seawater over the course of a Snowball  
553 Earth episode of 10 Myr duration. The shaded areas show typical (grey) and  
554 maximum (light grey) observed thicknesses: 3–30 m for  $\text{CaCO}_3$  (maximum  
555 400 m)<sup>12</sup>; and 1.5–38 m for  $\text{CaMg}(\text{CO}_3)_2$  (maximum  $>175$  m)<sup>52</sup>. The curves  
556 show the probability, based on all simulations, that a given thickness will be  
557 exceeded; e.g. for the full simulation (black line) shown in **(c)**, more than 40%  
558 of simulations exceed the observed mean of carbonate thickness ( $\sim 18.5$  m),  
559 and 20% exceed 30 m. Curves are shown for the full simulation (black line)  
560 and three alternative ridge productivity scenarios (I-III) defined in SI Table  
561 2.

562 **Figure 4 | Monte Carlo simulations for estimated phosphorus fluxes**  
563 **into a typical ‘snowball’ ocean.** Input parameter ranges are defined in  
564 Table 1. Note the logarithmic scale for the flux axis in (a). **a.** Flux of P,



565 accounting for CFA cementation (Supplementary Information Fig. 4). Solid  
 566 line denotes the modern annual dissolved riverine P flux for comparison<sup>37</sup>. **b.**  
 567 Probability of exceedance of phosphorus fluxes computed for the full simu-  
 568 lation (black line) and three alternative ridge productivity scenarios (I–III)  
 569 defined in SI Table 2 (see Supplementary Information Fig. 5 for the effects of  
 570 CFA cementation).

## 571 Tables

572 **Table 1 | Ranges of parameter values used in the Monte Carlo simula-  
 tions.** See Methods for further details.

Sampled parameters	Minimum value	Maximum value
$R$ = Ridge length (m) (ref. <sup>3</sup> )	$0.5 \times 10^7$	$2 \times 10^7$
$S$ = Spreading rate (m yr <sup>-1</sup> ) (refs. <sup>5,34,35</sup> )	0.05	0.2
$D$ = Alteration (penetration) depth (m) (ref. <sup>36</sup> )	100	1500
$H_s$ = Fraction hyaloclastite from 0–1 km depth (ref. <sup>23</sup> , Methods)	0.5	0.8
$\Phi_s$ = Hyaloclastite porosity ( $\Phi$ ) from 0–1 km depth (ref. <sup>36</sup> )	0.12	0.3
$H_d$ = Fraction hyaloclastite from 1–1.5 km depth (ref. <sup>23</sup> , Methods)	0.1	0.2
$\Phi_d$ = Hyaloclastite porosity ( $\Phi$ ) from 1–1.5 km depth (ref. <sup>36</sup> )	0.08	0.12
$P$ = Altered (palagonite) fraction (ref. <sup>24,25</sup> )	0.6	1.0
$L_{CaO}$ = Fraction CaO loss (ref. <sup>24,25</sup> )	0.04	0.1
$L_{SiO_2}$ = Fraction SiO <sub>2</sub> loss (ref. <sup>24,25</sup> )	0.1	0.3
$L_{P_2O_5}$ = Fraction P <sub>2</sub> O <sub>5</sub> loss (ref. <sup>24,25</sup> )	0.002	0.006
$L_{MgO}$ = Fraction MgO loss (ref. <sup>24,25</sup> )	0.027	0.067
$C_{CaO}$ , $C_{CFA}$ , $C_{SiO_2}$ , $C_{MgO}$ = Cement phase (as fraction of element loss)	0	1.0

573

## 574 Methods

575 Deposition of chemically easily weathered hyaloclastites will cause a major influx of  
 576 Ca, P, Si and Mg, among other elements, into the oceans. Monte Carlo simulations  
 577 were performed to capture the variation in the main depositional and weathering  
 578 processes. Input parameters were sampled independently from uniform distributions  
 579 over fixed intervals, given in Table 1 (using the Scythe C++ Statistical Library<sup>58</sup>).  
 580 Uniform distributions were chosen as these yield the most conservative estimate  
 581 of uncertainty, and there is not enough observational evidence to justify a more  
 582 tightly constrained distribution (e.g. specifying a central weighting would require  
 583 knowledge of the mean and variance of the distribution). The model generates a vol-  
 584 ume of hyaloclastite (m<sup>3</sup> yr<sup>-1</sup>), given a sampled total ridge length ( $R$ ), spreading  
 585 rate ( $S$ ) and cumulative deposit thickness ( $D$ ). The annual elemental flux estimates  
 586 (Figs 3a,b) are based on annual ridge output (fresh material along the hot ridge

587 axis). Any subsequent contributions from previously unaltered erupted products  
588 are conservatively excluded. Long-term accumulation in the ocean (over the period  
589 of active rifting) (Figs 3c,d) is estimated by summing the (variable) annual elemen-  
590 tal contributions over a period of 10 Myr, again a conservative estimate of the time  
591 during which we would expect extensive hyaloclastite formation and alteration. We  
592 therefore account for short-term fluctuations in calculating cumulative oceanic in-  
593 puts, and potential deposit (cap carbonate) thickness. The ridge length is varied  
594 from  $5\text{--}20 \times 10^3$  km to simulate progressive breakup of Rodinia around the perime-  
595 ter of Laurentia<sup>59</sup>. The spreading rate is varied from  $0.05\text{--}0.2$  m yr<sup>-1</sup> to simulate  
596 moderate<sup>60</sup> to fast<sup>61</sup> rates expected during breakup<sup>62</sup>. Here, the higher rate is not  
597 unreasonable, given that Laurentia is known to have moved at speeds of  $0.2$  m yr<sup>-1</sup>  
598 during the Ediacaran<sup>63</sup>.

599 Conservatively we consider a range of alteration penetration depths from 100–1500  
600 m<sup>64</sup>. Through analogy with ophiolite sequences, hyaloclastite deposit thickness and  
601 other parameters will vary with depth. In the upper kilometre, the hyaloclastite  
602 (i.e. pyroclastic) fraction ( $H_s$ ) ranges from 50–80% of the total bed depth, reflect-  
603 ing the observed tendency for enhanced explosivity in shallow water conditions (<1  
604 km)<sup>65,66</sup>. Below 1 km hyaloclastites are expected to be less extensive (10–20% of  
605 bed depth) due to an overriding tendency for intrusive processes at depth in ocean  
606 crust<sup>64</sup>. Again conservatively we assume no hyaloclastite below 1.5 km. These es-  
607 timates are consistent with deposits observed along analogous rifted margins<sup>67–70</sup>.  
608 The equations used in simulations are given below (for definitions, see Table 1 and  
609 Supplementary Information Tables 3 & 4).

610 Equation [2] gives the total thickness of hyaloclastite deposits, and [3] the cor-  
611 responding mass of hyaloclastite formed per year along the length of the ridge.  
612 Equation [4] gives the approximate mass of P<sub>2</sub>O<sub>5</sub>, CaO, SiO<sub>2</sub> or MgO lost due to  
613 hyaloclastite alteration. This can either be released to the ocean or consumed during  
614 cement formation.

$$\left. \begin{array}{l} t_s = DH_s \\ t_d = 0 \end{array} \right\} D \leq 1000 \text{ (m)} \quad (2)$$

$$\left. \begin{array}{l} t_s = 1000H_s \\ t_d = (D - 1000)H_d \end{array} \right\} D > 1000 \text{ (m)}$$

$$m_{total} = RS\rho_{crust}(t_s(1 - \Phi_s) + t_d(1 - \Phi_d)) \quad (3)$$

$$m_{P2O5/CaO/SiO2/MgO} = m_{total}PL_{P2O5/CaO/SiO2/MgO} \quad (4)$$

615 Hyaloclastite volume will also be affected by porosity, which below 1 km depth ( $\Phi_d$ )  
616 is taken to range from 0.08–0.12 (ref. 66), and above 1 km ( $\Phi_s$ ), where there is  
617 less compaction, from 0.12–0.3 (refs 64,71). Given that the volcanic environment

618 and regime will largely generate fine-grained glass particles, and considering the  
619 relatively high porosities and reactive surface areas, we consider an altered fraction  
620 ( $P$ ) ranging from 0.6–1.0, again typical of natural examples<sup>74</sup>. The resulting deposit  
621 is then subject to elemental losses (i.e., flux into the ocean and cement formation).  
622 For example, Ca losses ( $L_{CaO}$ ) are assumed to range from 0.04–0.1 of the altered  
623 fraction, as observed in natural samples<sup>72,73</sup>. These input distributions represent  
624 the main processes affecting annual variability in elemental flux.

625 A component of the elemental losses will form pore-filling cements and the remain-  
626 der is assumed to go directly into the ocean. Cement fraction ( $C_{CaO}$ ) is highly  
627 variable in nature<sup>71</sup>. We therefore allow it to range from 0–1.0 of the total amount  
628 of the leachate, and consider secondary phases that result in relatively high losses  
629 of elements. For calcium, we consider  $CaCO_3$  containing  $\sim 56\%$  CaO, while saponite  
630 clays (smectite) only contain  $\sim 1.2\%$  CaO. This approach leads to a conservative  
631 estimate of ocean flux, particularly as cement formation typically takes place over  
632 longer timescales ( $>10^5$  yrs)<sup>74,75</sup>.

633 The model considers the formation of (i) carbonate fluorapatite (CFA) cement, with  
634 equation [5] giving the mass of  $P_2O_5$  in cements, [6] the mass of CaO in cements,  
635 and [7] the total CFA cement mass; (ii) carbonate cement, with [8] giving the mass  
636 of CaO and [9] the total mass of  $CaCO_3$  cement; (iii) saponite clays, with [10] giving  
637 the total mass of  $SiO_2$  and [11] the total mass of saponite; and dolomite cement,  
638 with [12] giving the mass of MgO and [13] the total mass of  $CaMg(CO_3)_2$  cement.  
639 In all cases the resulting mass released to the ocean is assumed to be  $m^o = m - m^c$ .  
640 The numbers of moles of Ca, P, Si and Mg released to the ocean are given in [14],  
641 [15], [16] and [17]. Equation [18] gives the equivalent fraction of hyaloclastite pore  
642 space filled with cement or clay.

643 Carbonate fluorapatite (CFA) ( $kg\ yr^{-1}$ ):

$$m_{P_2O_5}^c = C_{CFA} m_{P_2O_5} \quad (5)$$

$$m_{CaO}^c = \left( \frac{0.56}{0.36} \right) m_{P_2O_5}^c \quad (6)$$

$$m_{CFA}^c = \frac{100 m_{P_2O_5}^c}{q_{P_2O_5}} \quad (7)$$

644 Carbonate cement ( $kg\ yr^{-1}$ ):

$$m_{CaO}^c = C_{CaO} m_{CaO} \quad (8)$$

$$m_{CaCO_3}^c = m_{CaO}^c + (w_{CO_2}^{mol} \left( \frac{m_{CaO}^c}{w_{CaO}^{mol}} \right)) \quad (9)$$

Saponite-type clays (kg yr<sup>-1</sup>):

$$m_{SiO_2}^c = C_{SiO_2} m_{SiO_2} \quad (10)$$

$$m_{saponite}^c = \frac{100 m_{SiO_2}^c}{q_{SiO_2}} \quad (11)$$

645 Dolomite cements (kg yr<sup>-1</sup>):

$$m_{MgO}^c = C_{MgO} m_{MgO} \quad (12)$$

$$m_{CaMg(CO_3)_2}^c = m_{MgO}^c + (2w_{CO_2}^{mol} + w_{CaO}^{mol}) \left( \frac{m_{MgO}^c}{w_{MgO}^{mol}} \right) \quad (13)$$

646 Flux to the ocean (mol yr<sup>-1</sup>):

$$n_{Ca} = m_{CaO}^o \left( \frac{1000}{w_{CaO}^{mol}} \right) \quad (14)$$

$$n_P = 2m_{P_2O_5}^o \left( \frac{1000}{w_{P_2O_5}^{mol}} \right) \quad (15)$$

$$n_{Si} = m_{SiO_2}^o \left( \frac{1000}{w_{SiO_2}^{mol}} \right) \quad (16)$$

$$n_{Mg} = m_{MgO}^o \left( \frac{1000}{w_{MgO}^{mol}} \right) \quad (17)$$

647 Pore fill:

$$f_{fill} = \left( \frac{m^c / \rho_{cement}}{(\Phi_s v_s) + (\Phi_d v_d)} \right) \quad (18)$$

648 Input parameter distributions are deliberately and conservatively wide to simulate  
649 the full range of plausible conditions and high temporal and spatial variability during

650 ridge formation. Ocean flux estimates for three variant scenarios, corresponding to  
651 (I) full unzipping with high hyaloclastite production, (II) full unzipping with moder-  
652 ate hyaloclastite production and (III) partial unzipping with moderate hyaloclastite  
653 production are presented to demonstrate model sensitivity to basic assumptions.  
654 Supplementary Information Table 2 presents the full range of input distributions  
655 for the full and variant scenarios.

656 Supplementary Information figure 3 shows the fluxes of (a) calcium and (b) phospho-  
657 rus into the ocean as a function of spreading rate and accumulated deposit thickness  
658 (using full simulation values in Supplementary Information Table 2). Supplemen-  
659 tary Information figure 4 shows estimated hyaloclastite volumes, and the effect of  
660 cementation on ocean flux of P. The specific effect of cementation on the phospho-  
661 rus flux was also considered (Supplementary Information Fig. 5), and shows that  
662 even cases involving high degrees of cement formation can still result in very high  
663 dissolved phosphorus fluxes (relative to the modern riverine flux) for long ridges.  
664 Supplementary Information figure 6 shows probability of exceedance for Ca and  
665 Si for the variant scenarios (I, II and III in Supplementary Information Table 2),  
666 alongside the full simulation.

667 A further simulation explores sensitivity to the temporal evolution of the rifting  
668 process, accounting for likely (but difficult to constrain) correlations between ridge  
669 length and magmatic productivity. Here we define three phases in the rifting pro-  
670 cess, based on the parameters used for the full simulation (observed global, present  
671 day averages): (A) Initiation, where ridge length is short ( $R = 5000\text{--}10000$  km) but  
672 productivity is high ( $S = 0.15\text{--}0.2$  m yr<sup>-1</sup>,  $D = 1000\text{--}1500$  m); (B) Mid-event ( $R = 10000\text{--}15000$  km,  
673  $S = 0.10\text{--}0.15$  m yr<sup>-1</sup>,  $D = 600\text{--}1000$  m); and (C) Final stages  
674 of rifting where the ridge has reached its full extent but productivity is very low  
675 ( $R = 15000\text{--}20000$  km,  $S = 0.05\text{--}0.10$  m yr<sup>-1</sup>,  $D = 100\text{--}600$  m). All other param-  
676 eters are as defined in Supplementary Information Table 2 for the full simulation.  
677 Supplementary Information figure 7 shows the probability of exceedance for annual  
678 Ca flux for phases A, B and C, compared to the full simulation (shown in black).  
679 This shows that although we cannot explicitly model correlations between param-  
680 eters (e.g. arising from temporal evolution), the full and variant scenarios provide  
681 a reasonable representation of cumulative fluxes over typical timescales associated  
682 with unzipping of Rodinia (order 10 Myr). Unfortunately, there is insufficient ob-  
683 servational evidence to apply covariance estimates to other parameters used in our  
684 simulations. In the absence of robust evidence, any attempt to correlate parameters  
685 (for example, cement fraction and depth) would decrease the uncertainty, thereby  
686 reducing the spread of the output distributions and providing false certainty in the  
687 outputs.

688 To reconcile the results of the simulation with observed post-snowball cap carbonate  
689 and dolostone deposits, we estimate the thickness of precipitates that could form  
690 after 10 Myr accumulation of oceanic Ca and Mg (Figs 3c-d). Taking the simulated  
691 annual flux of Ca and Mg (mol yr<sup>-1</sup>) as the average for the episode, and assuming  
692 a final deposition area equivalent to the modern day continental shelf ( $A = 2.8 \times$   
693  $10^{13}$  m<sup>2</sup>) gives the following estimate for cumulative deposit thickness after 10 Myr:

$$T = n^{mol} \times 10^7 \left( \frac{w^{mol}}{1000} \right) \left( \frac{1}{\rho A} \right) \quad (19)$$

694 where  $n^{mol}$  is the number of moles  $\text{yr}^{-1}$  from our simulation,  $w^{mol}$  is the molar  
 695 weight of either carbonate,  $\text{CaCO}_3$  ( $100 \text{ g mol}^{-1}$ ) or dolomite,  $\text{CaMg}(\text{CO}_3)_2$  ( $184.4$   
 696  $\text{g mol}^{-1}$ ), and  $\rho$  is the density of the deposit, i.e.  $\rho_{\text{CaCO}_3}$  or  $\rho_{\text{Dolo}}$  (Supplementary  
 697 Information Table 4).

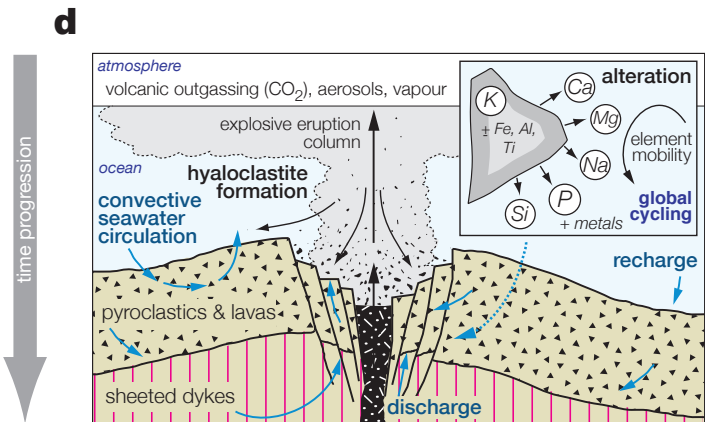
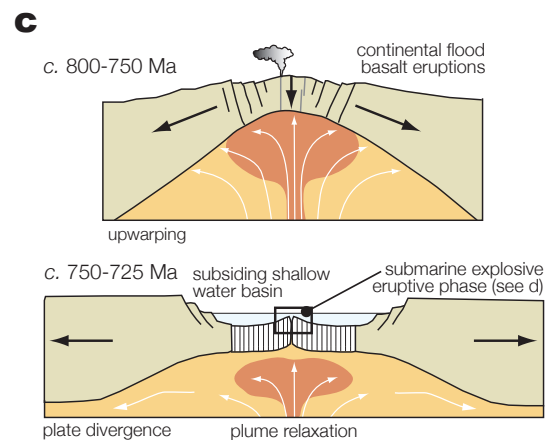
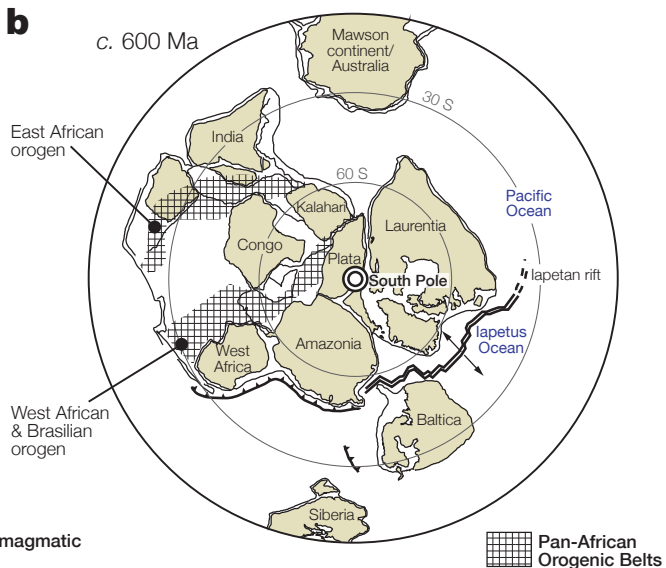
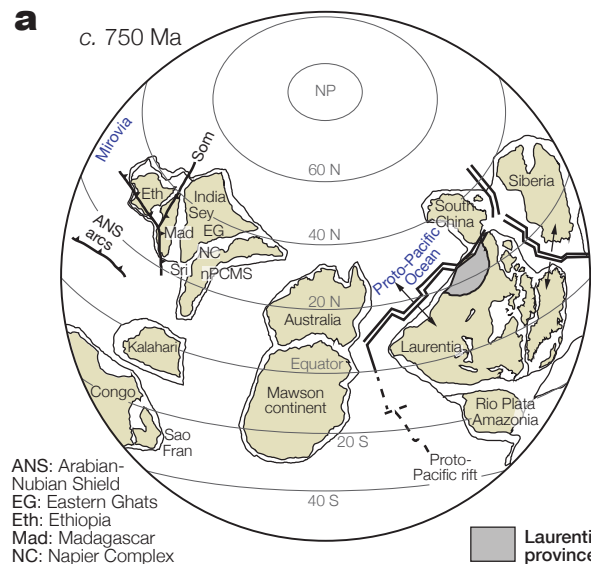
## 698 Code availability

699 We have opted not to make the computer code associated with this paper available  
 700 because it is currently being developed for another follow-up study, but will be  
 701 released when this work is published.

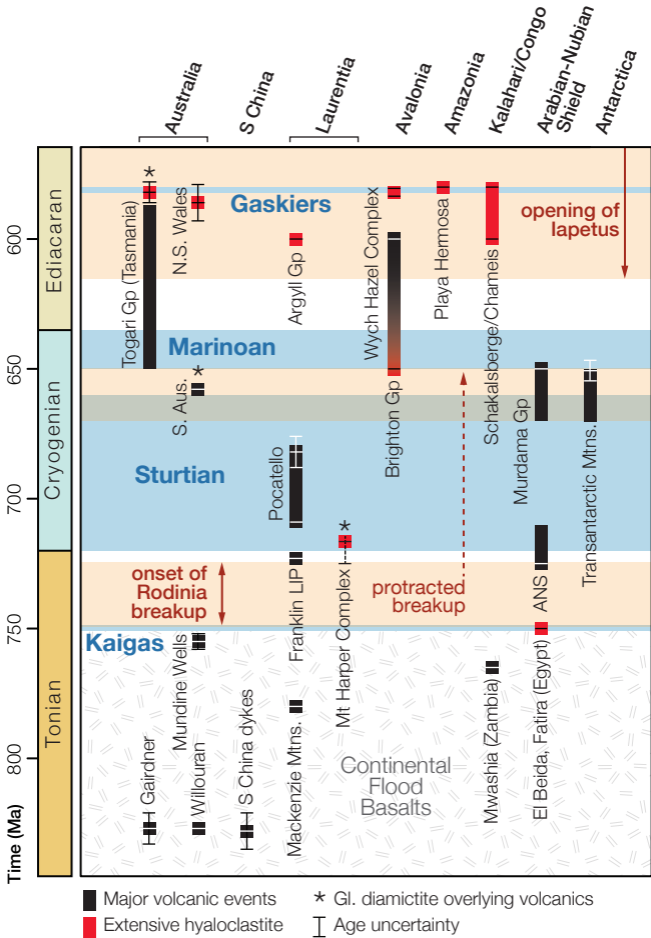
## 702 Methods references

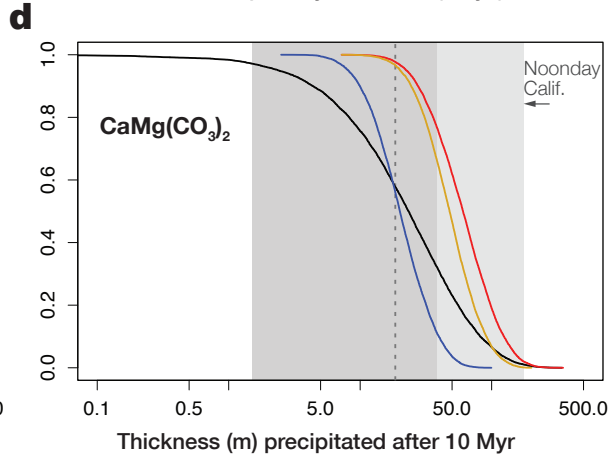
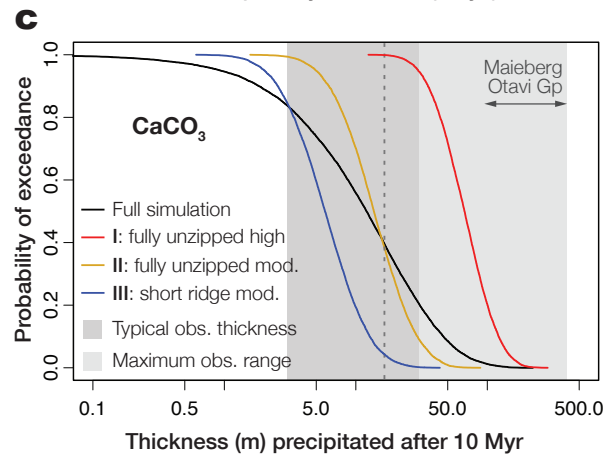
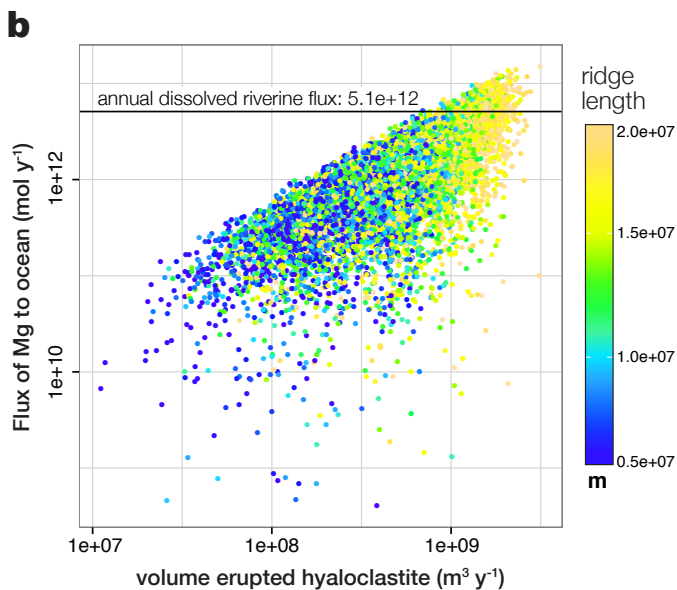
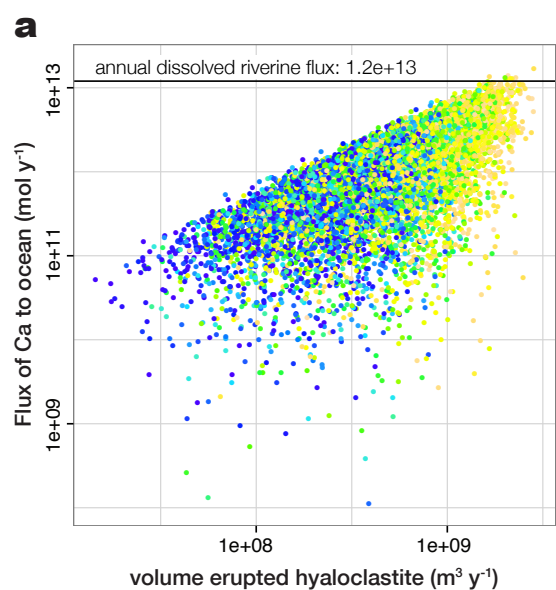
- 703 (58) Pemstein, D., Quinn, K. M., and Martin, A. D. The Scythe Statistical Li-  
 704 brary: An Open Source C++ Library for Statistical Computation. *Journal of*  
 705 *Statistical Software* **42**, 1–26 (2011)
- 706 (59) Eyles, N. and Januszczak, N. ‘Zipper-rift’: a tectonic model for Neoproterozoic  
 707 glaciations during the breakup of Rodinia after 750 Ma. *Earth-Science Reviews*  
 708 **65**, 1–73 (2004).
- 709 (60) Reid, I. and Jackson, H. R. Oceanic spreading rate and crustal thickness.  
 710 *Marine Geophysical Researches* **5**, 165–172 (1981).
- 711 (61) Wilson, D. S. Fastest known spreading on the Miocene Cocos-Pacific Plate  
 712 Boundary. *Geophysical Research Letters* **23**, 3003–3006 (1996).
- 713 (62) Storey, M., Duncan, R. A., and Tegner, C. Timing and duration of volcanism in  
 714 the North Atlantic Igneous Province: Implications for geodynamics and links  
 715 to the Iceland hotspot. *Chemical Geology* **241**, 264–281 (2007).
- 716 (63) Torsvik, T. H., Smethurst, M. A., Meert, J. G., Van der Voo, R., McKerrow,  
 717 W. S., Brasier, M. D., Sturt, B. A., and Walderhaug, H. J. Continental break-  
 718 up and collision in the Neoproterozoic and Palaeozoic —A tale of Baltica and  
 719 Laurentia. *Earth-Science Reviews* **40**, 229–258 (1996).
- 720 (64) Alt, J. C. Subseafloor Processes in Mid-Ocean Ridge Hydrothermal Systems.  
 721 In: *Seafloor Hydrothermal Systems: Physical, Chemical, Biological, and Geo-*  
 722 *logical Interactions*, Humphris, S. E., Zierenberg, R. A., Mullineaux, L. S., and  
 723 Thomson, R. E., editors, **91**, 85–114. American Geophysical Union (1995).
- 724 (65) Fisher, R. V. Submarine volcanoclastic rocks. *Geological Society, London, Spe-*  
 725 *cial Publications* **16**, 5–27 (1984).

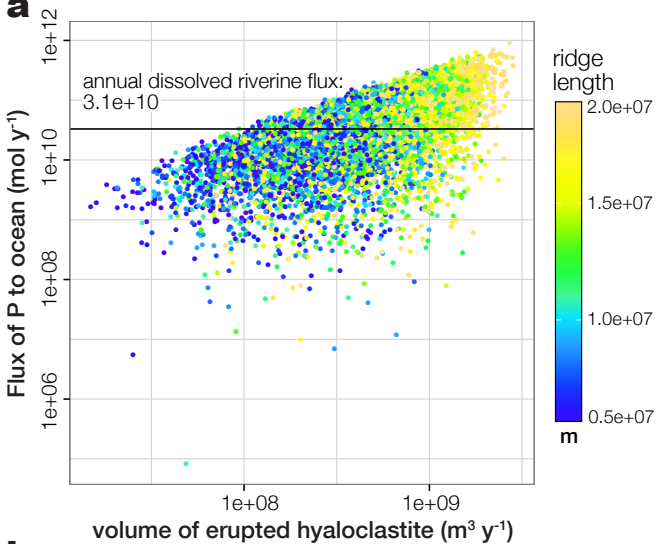
- 726 (66) Batiza, R. and White, J. D. L. Submarine lavas and hyaloclastite. In: Ency-  
727 clopedia of Volcanoes, Sigurdsson, H., editor, 361–381. Academic Press, San  
728 Diego (2000).
- 729 (67) Planke, S., Symonds, P. A., Alvestad, E., and Skogseid, J. Seismic volcanos-  
730 tratigraphy of large-volume basaltic extrusive complexes on rifted margins.  
731 *Journal of Geophysical Research* **105**, 19335–19351 (2000).
- 732 (68) Peate, I. U., Larsen, M., and Leshner, C. The transition from sedimentation  
733 to flood volcanism in the Kangerlussuaq Basin, East Greenland: basaltic py-  
734 roclastic volcanism during initial Palaeogene continental break-up. *Journal of*  
735 *the Geological Society* **160**, 759–772 (2003).
- 736 (69) Bell, B. and Butcher, H. On the emplacement of sill complexes: evidence  
737 from the Faroe-Shetland Basin. *Geological Society, London, Special Publica-*  
738 *tions* **197**, 307–329 (2002).
- 739 (70) Jerram, D. A., Single, R. T., Hobbs, R. W., and Nelson, C. E. Understanding  
740 the offshore flood basalt sequence using onshore volcanic facies analogues: an  
741 example from the Faroe–Shetland basin. *Geological Magazine* **146**, 353–367  
742 (2009).
- 743 (71) Walton, A. W. and Schiffman, P. Alteration of hyaloclastites in the HSDP 2  
744 Phase 1 Drill Core 1. Description and paragenesis. *G3* **4**, 8709 (2009).
- 745 (72) Stroncik, N. A. and Schmincke, H. U. Palagonite – a review. *International*  
746 *Journal of Earth Sciences* **91**, 680–697 (2002).
- 747 (73) Staudigel, H. and Hart, S. R. Alteration of basaltic glass: mechanisms and sig-  
748 nificance for the oceanic crust-sea water budget. *Geochimica et Cosmochimica*  
749 *Acta* **47**, 337–350 (1983).
- 750 (74) Morton, A. C. and Keene, J. B. Paleogene pyroclastic volcanism in the south-  
751 west Rockall Plateau - Deep Sea Drilling Project Leg 81. In: *DSDP Initial*  
752 *Reports*, volume 81, chapter 19, 633–643. (1984).
- 753 (75) Desprairies, A., Bonnot-Courtois, C., Jehanno, C., Vernhet, S., and Joron, J. L.  
754 Mineralogy and geochemistry of alteration products in leg 81 basalts - Deep  
755 Sea Drilling Project (Rockall Plateau). In: *DSDP Initial Reports*, volume 81,  
756 chapter 28, 733–742. Ocean Drilling Program (1984).









**a****b**